ELSEVIER

Contents lists available at ScienceDirect

Chemical Engineering Journal

journal homepage: www.elsevier.com/locate/cej





In situ 3D printing of implantable energy storage devices

Vaishali Krishnadoss ^a, Baishali Kanjilal ^{a,b}, Alexander Hesketh ^a, Caleb Miller ^a, Amos Mugweru ^c, Mohsen Akbard ^d, Ali Khademhosseini ^{e,f}, Jeroen leijten ^g, Iman Noshadi ^{a,b,*}

- ^a Department of Chemical Engineering, Rowan University, Glassboro, NJ 08028, USA
- ^b Department of Bioengineering, University of California, Riverside, CA 92521, USA
- ^c Department of Chemistry and Biochemistry, Rowan University, Glassboro, NJ 08028, USA
- ^d Department of Mechanical Engineering, Victoria University, Victoria, BC, Canada
- ^e Center for Minimally Invasive Therapeutics (C-MIT), California NanoSystems Institute (CNSI), UCLA, 4121D Engineering V, Los Angles, CA 90095, USA
- f Terasaki Institute for Biomedical Innovation, Los Angles, CA
- g Department of Bioengineering, TechMed Centre, University of Twente, Enschede 7522 NB, Netherlands

ARTICLEINFO

Keywords: Biocompatible Hydrogels Energy Storage Devices Bio Ionic Liquid In Situ 3D printing

ABSTRACT

The increasing demand for wearable bioelectronic devices has driven tremendous research effort on the fabrication of bioelectronics in microscale. To ensure the functionality and reliability, wearable bioelectronics need to be integrated with independent and internal energy storage systems to avoid frequent charging process from external sources. The supercapacitors has been considered as an electric energy source due to benefits such as a long cycle life, a high power density and fast charge-discharge rate. Miniaturization, biocompatibility, and biodegradability are the primary keys to achieving the requisites for implantable supercapacitors. Rapid, in situ 3D printing of implantable bioelectronic devices can address these needs. However, in situ 3D printing of bioelectronics using currently available materials has remained challenging due to their suboptimal physicochemical properties. Here, we present a novel material platform based on bio ionic liquid (BIL) functionalized biopolymers which can form a hydrogel electrolyte when exposed to visible light. Fine-structure, interdigitated, biocompatible, and implantable soft micro-supercapacitors (MSC) were created by 3D in situ bioprinting of these polymer electrolytes in combination with rheologically optimized graphene hydrogel-laponite (GH-L) blend as electrode material. The hydrogel electrolyte had a specific capacitance of $\sim 200 F/g$, while the MSC had a specific capacitance of $\sim 16 \,\mu\text{F/g}$ at a current density of 1 A/g, volumetric capacitance of $\sim 44 \,\mu\text{F/cm}^3$, cyclic stability up to 10,000 cycles, energy densities nearly as high as implantable batteries, and a power density level of implantable supercapacitors. This novel material platform enables in situ 3D printing of flexible bioelectronics structures with integrated life-long power source.

1. Introduction

Advancements in materials and fabrication technology have enabled the fabrication of bioelectronic devices, which has allowed for the integration of wearable bioelectronics devices with living tissue [1-3]. Current techniques have largely focused on bypassing restrictions imposed by thermal and mechanical considerations of traditional microfabrication [4]. Despite the development in additive manufacturing, it has remained challenging to 3D print functional devices with intricate structural details on undulating surfaces such as natural living tissues, which has hindered the integration of 3D printed bioelectronics with biological systems [5-7]. Such integrative processes

will require closed-loop scan-and-print procedures as well as the development of bio-inks with processability under conditions conducive to cellular growth and bodily acceptance [8,9]. Furthermore, a soft, biocompatible, lightweight, and durable energy source is imperative for the development of miniaturized implantable bioelectronics for advanced personalized healthcare applications [10,11].

Biocompatible MSCs with high-power density, and a fast charge—discharge rate are ideally suited for applications to power implantable bioelectronics such as pacemakers and sensors [12-15]. Traditional batteries are larger in size and can potentially leak highly toxic fluids into surrounding tissues. Moreover, weak energy autonomy and costly maintenance make batteries impractical for implantable devices [16-

^{*} Corresponding author at: Department of Bioengineering, University of California, Riverside, CA 92521, USA. *E-mail address:* imann@ucr.edu (I. Noshadi).

18]. To capitalize on the potential of MSCs, novel materials and engineering designs for in situ 3D printed implantable energy storage devices are vital. Specially, such materials will need to combine high energy density, strength to weight ratio, and biocompatibility, and allow for scalable, rapid, and complex miniature fabrication [19-21]. Electrochemically active 3D printable material platforms are also expected to be of value to additional fields such as regenerative medicine by advancing the engineering of electrically conductive cardiac or neural tissues [22-24].

To resolve this challenge, we introduce a new biocompatible electrolyte material platform based on the functionalization of cross linkable polymers with BIL, which offers novels materials with highly relevant physico-mechanical, cytocompatible, and energy storage properties. Here, choline based BIL was used to showcase and functionalize polymeric backbones of two biocompatible polymers – one natural and one synthetic - with resultant enhancement in the physical and capacitive properties of the polymers. The resultant electrochemical properties and energy densities were very close to those of batteries while achieving power density of mid-range supercapacitors, which underlining its potential applications as ionic gel electrolyte. The robust rheo-mechanical and biocompatible properties of the electrolyte material platform enabled the straightforward 3D bioprinting of tailored complex structures, allowing for the rapid prototyping of bio-implantable electronics including MSCs. In addition to the electrolyte, we also designed and optimized electrochemical and rheological properties of GH-L composite, which was used as a 3D printable material to create electrodes [25-27]. A multi material construct composed of BIL functionalized polymers and GH-L was 3D printed into interdigitated soft MSC prototype structures with excellent electro-mechanical and energy storage properties. Subcutaneous implantations were performed to investigate the 3D printed soft MSC biocompatibility and in-vivo integration. Our work demonstrates the possibility of using the BIL functionalized polymer as a tailorable and robust electrolyte material platform for scalable in situ 3D printing of implantable energy storage devices that can potentially be utilized as biomedical devices and implants for healthcare applications.

2. Materials and methods

2.1. Polymer electrolyte and electrode synthesis

The synthesis of the polymer electrolyte entailed mixing the methacrylated polymer and choline acrylate, BIL in various ratios. Choline bitartrate and acrylic acid were reacted, at 50 °C for a duration of 5hr, in a 1:1 mol ratio, to obtain the BIL, which was washed using ethyl acetate and dried by rotary evaporation and freeze drying to make the choline acrylate BIL. The BIL was grafted on gelatin methacryloyl (GelMA) and polyethylene glycol diacrylate (PEGDA) polymers to make BIL-GelMA (BG) and BIL-PEGDA (BP) hydrogels respectively. GelMA was synthesized in reference to a previously described method. Gelatin solution of 10% (w v⁻¹) concentration and 8 mL of methacrylic anhydride were reacted for 3 h. The unreacted anhydride was dialyses out for 5 days and the resultant product frozen at - 80 °C freezer for 24 h. This was followed by freeze-drying the frozen acrylated polymer for 7 days. PEGDA was obtained from Sigma Aldrich (average M_n 700). The Bio Ionic polymer electrolyte series BG and BP were made by using 20%(w v⁻¹) solution of prepolymer in distilled water to which varying BIL at a 0, 5 10, 15 and 20%(w v⁻¹) concentration were added along with 0.5%(w v⁻¹) of Lithium phenyl-2,4,6-trimethylbenzoylphosphinate (LAP) as a photo initiator and visible light 405 nm for 60 s.

The electrode is fabricated using reduced graphene oxide synthesized by previously described methods [28]. Briefly, a 9:1 mixture of concentrated $\rm H_2SO_4/H_3PO_4$ (360:40 mL) was added to a mixture of 3.0 gm of graphite flakes and 18 gm of KMnO₄ the reaction was then heated to 50 °C and stirred for 12 h. The reaction was cooled to room temperature and poured onto ice (400 mL) with 3 mL of 30% hydrogen peroxide. For workup, the mixture was sifted through a 300- μ m metal U.

S. Standard testing sieve and then filtered through polyester fiber. The filtrate was centrifuged at 4000 rpm for 4 h, and the supernatant was decanted away. The remaining solid material was then washed in succession with 200 mL of water, 200 mL of 30% HCl, and 200 mL of ethanol, obtained solid was vacuum-dried overnight at room temperature forming graphene oxide. Further, the graphene hydrogel was prepared using a modified hydrothermal reduction method [25]. Briefly, 0.3 mL of 2 M ascorbic acid aqueous solution was added into 6 mL of 4 mg/mL GO aqueous dispersion, and the mixture was sealed in a Teflonlined autoclave and maintained at 180C for 2 h. The autoclave was naturally cooled to room temperature, and graphene hydrogel was taken out with a tweezer and immersed in 1 M $_{\rm 2SO_4}$ aqueous solution overnight for the following experiments.

2.2. HNMR analysis of electrolyte

The 1 H NMR was carried out on a Varian Inova-500 spectrometer. Spectra of choline bitartrate, BIL, GelMA prepolymer, and Gel electrolytes were recorded. Peaks at $\delta=5.3$ and 5.7 ppm indicated methacrylate groups. The reduction in C = C double bond signal strength ($-\partial$ (C = C) ∂ t) of the GelMA methacrylates indicated the crosslinking extent of composite hydrogel and BG conjugation. The decrease in area was imputed as follows:

Decay of Methyl group
$$\% = [(PA_b - PA_a)/PA_b] * 100$$
 (1)

 PA_b and PAa represent the areas of methacrylate group peak before and post photocrosslinking, respectively. PA_b - PAa represents the methacrylated groups that were consumed by photocrosslinking. Mnova NMR analysis software integrated area under the peaks. The data was analyzed vis-a-vis phenyl peaks at $\delta=6.5$ –7.5 ppm.

2.3. Mechanical characterization of electrolyte

The elastic and compressive moduli of the gel electrolyte, of various compositions, were measured and analyzed. The hydrogel specimens were made using PDMS molds, designed for tensile tests. For compression tests, cylindrical hydrogels of 5.5 mm diameter and 4 mm height were molded. Before testing, the hydrogels were put in DPBS and swelled for 2 h at 37 $^{\circ}$ C, and 5 samples were tested for each condition.

For compression tests entailed the cylindrical specimens were compressed at a rate of 1 mm min $^{-1}$ between compression plates, while the compressive strain and the stress were recorded. Compression modulus was computed form the initial tangential slope between strain values of 0 mm mm $^{-1}$ and 0.1 mm mm $^{-1}$. Tensile testing employed hydrogel samples, clenched between tensile grips, were stretched at 1 mm min $^{-1}$ unto failure point. The elastic modulus was similarly computed for the initial slow of the stress–strain curve. Each data point consisted of the test results from at least 5 samples.

2.4. Brunauer-Emmett-Teller (BET) surface area analysis

To determine the surface areas and pore size distributions of the reduced graphene oxide, the graphene hydrogel was freeze-dried using a lyophilizer overnight and the N2 adsorption and desorption analyses were measured using a NOVA Touch LX4 Surface Area Analyzer (Quantachrome, Boynton Beach, FL, USA)

2.5. 3D printing of the energy storage device

Allevi 2 bioprinter (an extrusion-based bioprinter) was used for 3D-printing the bio ink. First, the interdigitation patterns were designed in SolidWorks and converted to G-code to ensure compatibility with the printer. The bio ink inside the syringe was deposited through a nozzle via air pressure to print out the desired pattern. The resolution was optimized based on the printing speed 6 mm/sec and the Extrusion

Pressure was maintained Constant at 70 psig.

2.6. In vitro degradation study on electrolyte

For the degradation tests, the electrolyte sample were fabricated as per previously described methods for compression tests, followed by freeze-drying. The weighed samples were dipped in 1 mL DPBS in 24 well plates at 37 $^{\circ}$ C for 2 weeks, refreshing the buffer solution every three days. The buffer solution was removed after 1, 7, and 14 days, samples freeze-dried for 24 h and weighed.

2.7. Evaluation of swelling ratio of electrolyte

To evaluate the equilibrium swelling of electrolytes, cylinder-shaped specimens were prepared as described above and washed thrice with DPBS, lyophilized, and weighed under dry conditions. The test specimens were immersed in DPBS at 37 $^{\circ}$ C. They were weighed at 4, 8 and 24 h after immersion. The water uptake and swelling ratio were computed as the ratio of the masses of the swelled and lyophilized samples.

2.8. SEM analysis

The porosity of the electrolytes was evaluated by SEM. The samples were prepared similar to that described in mechanical tests. The freezedried samples were coated with gold before imaging, where the images were acquired by Phenom. The pore size of the electrolytes was measured from at least 3–4 images using ImageJ software.

2.9. Electrochemical measurements of electrolyte and electrode

Electrochemical properties of the electrolytes, electrode and MSC were measured by cyclic voltammetry (CV), galvanostatic charge/discharge, and impedance spectroscopy. The instrument used was a CHI 660 potentiostat from CH Instruments, Inc., a three-electrode system was used for the measurements. CV was carried out between 0 and 1 V. The galvanostatic charge/discharge tests were carried out between -1V to +1 V. EIS was carried out between a 10^5 –0.05 Hz frequency range with an open circuit potential amplitude of 10 mV and varying scan rate from 10-200 mV sec^{-1} . Mass-specific capacitance (C) was computed as follows:

$$C = (I\Delta t/m\Delta V) \tag{2}$$

I is the constant discharge current, Δt , the discharging time, m, the mass of one electrode, and ΔV is the voltage drop upon discharging (excluding the IR drop). The Ragone plot was used to compute Energy and power densities (E & P, respectively) using equation (3):

$$E = (1/8)C \Delta V^2$$
 (3)

$$P = E/\Delta t \tag{4}$$

2.10. In vitro biocompatibility of the electrolyte

C2C12 at a cell density of $2\times 10^4 cells$ scaffold 1 were seeded on the electrolyte surface and fabricated device surface. These were placed in 24-well plates with 500 μl of DMEM mixed with 10% fetal bovine serum as growth medium. The 2D cultures were kept for 7 days at 37 $^{\circ} C$ and 5% CO $_2$ humidified atmosphere. The medium was changed every 48 h. The viability of primary C2C12 growth on electrolyte and fabricated device surfaces were evaluated by a commercial Invitrogen live/dead viability kit. Tests were carried out as per manufacturer's instructions. Staining was done with 0.5 μl ml $^{-1}$ calcein AM and 2 μl ml $^{-1}$ ethidium homodimer-1 (EthD-1) in DPBS for 15 min at 37 $^{\circ} C$. The fluorescent

images were taken on 1st, 4th, and 7th day after seeding. The AxioObserver Z1 inverted microscope from Zeiss was employed for imaging. While viable cells were green, apoptotic or dead cells appeared red. Their numbers were estimated using ImageJ. The number ratio of live cells to the total of live and dead cells was designated as the cell viability ratio.

The metabolic cellular activity was evaluated at 1,4 and 7 days after seeding, by a PrestoBlue fluorescence assay from Life Technologies as per manufacturer's instructions. 2D culture of C2C12 was incubated in 400 μl of 10% PrestoBlue reagent for 2 h at 37 $^{\circ} C$. The measurements were carried out at 560 nm (excitation) and 590 nm (emission), using a SpectraMax. The background was determined using control wells without cells.

The surface spreading was visualized using fluorescent staining of Factin filaments and cell nuclei. A 0.1% PBT, fresh fix solution containing 4% PFA in 0.1% PBT was prepared. The staining solution consisted of DAPI and phalloidin in PBS at a 1:1000 dilution. The cells were removed from the media and dispensed into 150 μl well $^{-1}$ of 1x PBS, into each 12-well plate. The PBS was removed by shaking out. 150 μl well $^{-1}$ of fix solution was dispenses and the cells fixed for 25 min. The fix solution was dispensed by shake out method. Around 200 μl well $^{-1}$ of PBT was dispensed and incubated for 5 min. It was shaken out and the process repeated for a total of 3 washes. PBS was removed by shake out method and to these 50 μl well $^{-1}$ of 1x PBS was added to keep the cells hydrated while imaging. Fluorescent images were obtained using Axio Observer Z1 inverted microscope.

2.11. In vivo degradation and compatibility

The animal experiments were approved by ICAUC (protocol 2018–004) at Rowan SOM following regulations. The animals - Male Wistar rats (200–250 g) were procured Charles River (Boston, MA, USA) and housed under circadian rhythm conditions in the local animal care facility. 4.0% isoflurane induction caused anesthesia, along with 2–2.5% maintainance, and 0.02 to 0.05 mg kg $^{-1}$ SC buprenorphine administration. On the posterior medic-dorsal skin eight 1-cm incisions were made. Lateral subcutaneous pockets cut out by blunt dissection around the incisions. The fabricated MSC's in the form of 5 \times 5 mm disks were implanted in the pockets. The anatomical wound was closed, and the animal allowed to recover from anesthesia. The animals were euthanized after 4,14 and 28 days by anesthesia or exsanguination. The implanted samples and associated tissue were recovered.

2.12. Histological analysis and immunofluorescent staining

Explanted hydrogel samples were cryosection and histologically analyzed to characterize inflammatory response. The samples were incubated at room temperature for 4 h in 4% paraformaldehyde after explantation, then incubated overnight at 4 °C, in 30% sucrose. The samples were embedded in Optimal Cutting Temperature compound (OCT). They embedded samples were flash frozen in liquid nitrogen and sectioned by a Thermofisher Cryostat. The cryosections of 15-µm dimensions so obtained were mounted in positively charged slides and stained with hematoxylin and eosin staining as per manufacturer's instructions. Immuno-histo fluorescent staining carried out on these cryosections used where anti-CD68 as primary antibodies. They were detected by Alexa Fluor 594-conjugated secondary antibody. Invitrogen's DAPI was used to counterstain these sections. They were imaged using AxioObserver Z1 microscope from Zeiss.

3. Results and discussion

Synthesis and Chemical Characterization of flexible electrolyte. BIL functionalized hydrogel electrolyte was synthesized from Choline acrylate and biocompatible polymer GelMA [29] or synthetic polymer PEGDA (average $M_{\rm n}$ 700) reaction. Choline derivatives with low melting

points have been used as ionic liquids. Mixtures of choline and other salts yield viscous liquids that conducts at or around room temperature [30,31]. Lecithin, found in plants and animals, constitutes Choline Bitartrate. It is an acetylcholine precursor and acts as a methyl donor in lipid metabolism [32]. Choline Bitartrate can be efficiently converted into Choline Acrylate Fig. 1, which we refer to as the BIL, BIL can be conjugated to GelMA and PEGDA. There is also a simultaneous linking of GelMA-GelMA (or PEGDA-PEGDA) chains leading to an increase in molecular weight and light crosslinking. BIL conjugation of the polymers was carried out by mixing 20%(w v-1) GelMA or 20%(v v-1) PEGDA with the BIL at a 0, 5 10, 15 and 20%(w v-1) concentration at room temperature to form BG (BG-0, BG-5, BG-10, BG-15, BG-20) and BP (BP-0, BP-5, BP-10, BP-15, BP-20). The resulting polymer/BIL was photo cross-linked into the electrolyte gel using LAP (Lithium phenyl-2,4,6trimethylbenzovlphosphinate) initiator, and visible blue light for 60 secs. Fig. 1 depicts, schematically, the synthesis and fabrication of the electrolyte materials, and the MSC structures-based BG and BP polymers. (Fig. 1 a) depicts the synthesis of BIL, (Fig. 1 b) depicts the formation of BG and BP. (Fig. 1 c) is a representation of the synthesis of GH-L composite by physical mixing. (Fig. 1 d) schematically represents the fabrication of 3D printed interdigitated MSCs structure.

Structural analysis based on FTIR and ¹H NMR confirmed the acrylation of the choline bitartrate, this resulted in choline acrylate as well as successful conjugation of BIL to the polymers (Fig. S1). The acrylate peak at 1720 cm⁻¹ in the IR spectrum confirms the choline bitartrate was acrylated to form with choline acrylate. Further, the hydrogen atom in acrylate group has been indicated at 5.8 - 6.3 ppm in ¹H NMR (Fig. S1 b) substantiating the synthesis of choline acrylate. In addition, BG was analyzed by ¹H NMR analysis indicating the disappearance of the methacrylamide group caused by crosslinking GelMA polymer chains as well as conjugation of the BIL to the polymer. The characteristic peaks at ~ 5.7 ppm and ~ 6.1 ppm indicated the conjugation of the polymer and BIL. This peak was absent in the non-BIL conjugated polymer. The sharp peak at $\delta \sim 3.1\text{--}3.2$ ppm that appeared in the conjugated polymer, corresponds to the three cholinium (ammonium ion) hydrogen atoms, further confirming BIL conjugation to the polymer.

Scanning electron microscopy (SEM) images as shown in (Fig. S1 c, d) revealed that GelMA and PEGDA polymers were porous. The SEM images of the BG and BP polymers with varying BIL concentration is shown in (Fig. S2). The porosity varies with the concentration of the BIL

in the polymer which indicated that the polymer's porosity can be tailored to control its global ion transport.

Physical and Mechanical characterization of the flexible electrolyte. The swelling ratio and the degradation rates of the gel electrolytes were determined (Fig. 2 a-d). Polymer compositions, irrespective of BIL percent, exhibit a similar pattern of water uptake, a rapid initial uptake leading to an equilibrium swelling level [33]. BG-0 exhibits the fastest rate of water uptake and maximum equilibrium swelling level. The maximum swelling ratio of GelMA with 0% BIL, increases from $73.9\%\pm$ 2.5% at 1hr to $159\%\pm5\%$ at 24hrs after incubation while for BG-20 they are 34.4%±3.4% at 1hr, increasing to 50.7%±8.7% at 24hrs after incubation. Polymers with 5-20% BIL take up water gradually. Water absorption by a polymer depends upon chain conformation and overlapping correlation blob formation in semi-dilute solutions [34,35]. For BG-0, these blobs open in water easily, allow more water until crosslinking prevents further physical expansion and water uptake. With BIL functionalization, strong electrostatic interactions ensue inside correlation blobs and between correlation blobs acting as physical "crosslinks", resisting polymer expansion. The density of crosslinking limits the final extent of swelling. A similar trend was seen with BIL incorporated

Degradation studies were also carried out on the gels. BG-0 shows the degradation of $7.3\%\pm0.7\%$ at day 1, increasing to $14\%\pm1\%$ on day 14. These values are $24\%\pm0.8\%$ (day 1) and, $32\%\pm1.0\%$ (day 14) for BG-20. With higher BIL content, the initial degradation is greater but the rate of degradation with 0%BIL is greater than that with 20% BIL for both GelMA and PEGDA. Hydrogel swelling plays a key part in degradation [36-38]. The quaternary ammonium head in choline may catalyze hydrolysis of the functionalities in the GelMA and PEGDA backbone causing degradation.

The mechanical strength of hydrogel has a vital role in solid-state supercapacitors. An increase in the BIL content from 0 to 5 (% w v $^{-1}$) causes nearly 50% increase in compressive modulus (Fig. 2 e-h). The compressive modulus of BG-20 content is 8 times higher than unfunctionalized polymer BG-0. BG-0 has compression modulus of 12.8 ± 1.5 kPa and a tensile modulus of 139 ± 28 kPa, whereas in BG-20 they increase to 190 ± 4 kPa and 455 ± 5 kPa respectively. Similarly, BP-0 has compression and tensile moduli of 8.64 ± 1.18 kPa and 96.5 ± 6.5 kPa whereas, with BP-20 the moduli increase to 74.5 ± 3.0 kPa and 284.7 ± 5.7 kPa respectively. Thus, mechanical properties can be modulated with BIL concentrations to fabricate the device differently. The

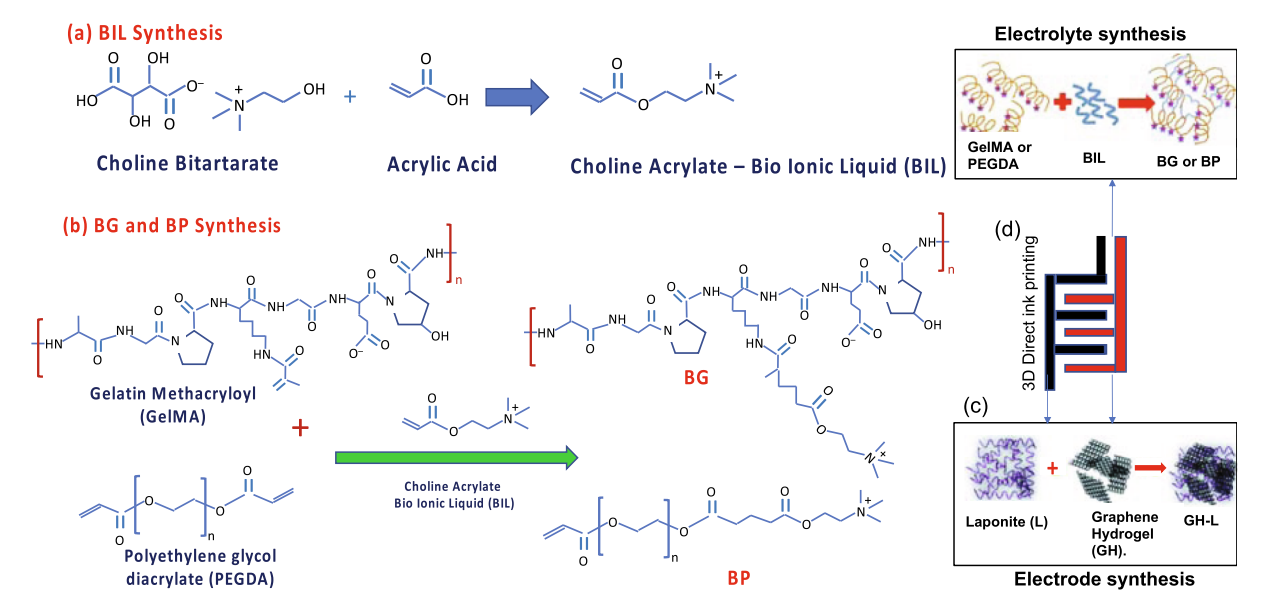


Fig. 1. Synthesis and fabrication schematics of soft BG-MSC and BP-MSC (a) Synthesis of BIL, (b) BG and BP (c) Synthesis of the GH-L composite. (d) Fabrication of MSCs: BG or BP as electrolyte and GH-L as electrode forming an interdigitated structure.

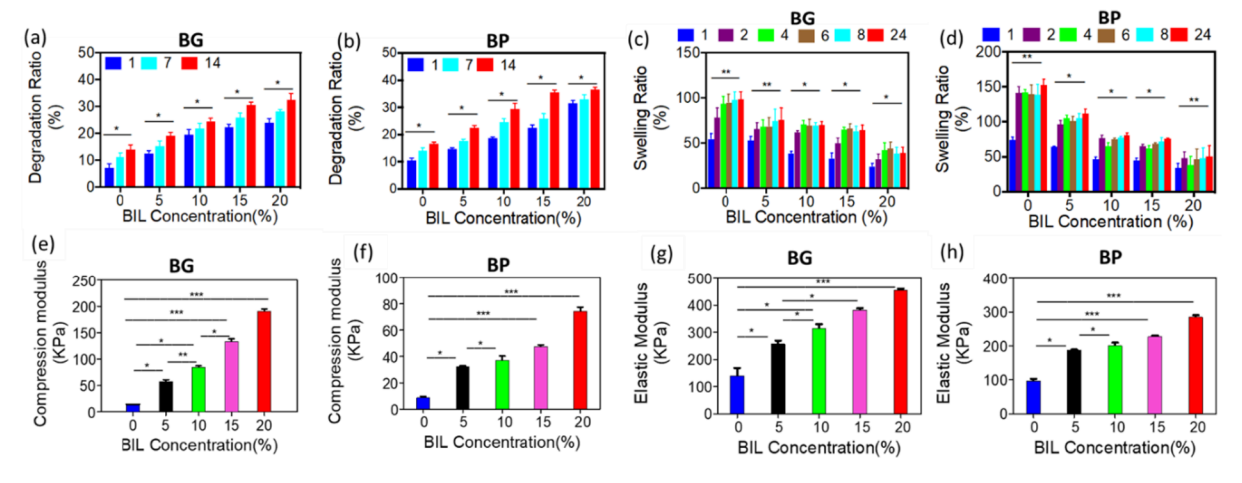


Fig. 2. In vitro swelling, degradation, and mechanical properties of gel electrolyte prepared by polymerization using photo-initiator and visible light: (a) Degradation of GelMA with varying BIL concentration (b) Degradation of PEGDA with varying BIL concentration. (c) Swelling ratio of GelMA with varying BIL concentration (d) Swelling ratio of PEGDA with varying BIL concentration. All *In vitro* Degradation and Swelling measured with 20(w/v) % polymer solutions in DPBS (e) Compression Modulus of BG Vs BIL concentration (f) Compression modulus of BP Vs BIL concentration. (g) Elastic Modulus of BG Vs. BIL concentration (h) Elastic Modulus of BP Vs. BIL concentration. Mechanical properties measured on 20(w/v) % polymer solution in DPBS. Error bars indicate standard error of the means, asterisks mark significance levels of p < 0.05 (*), p < 0.01 (***), and p < 0.001 (***).

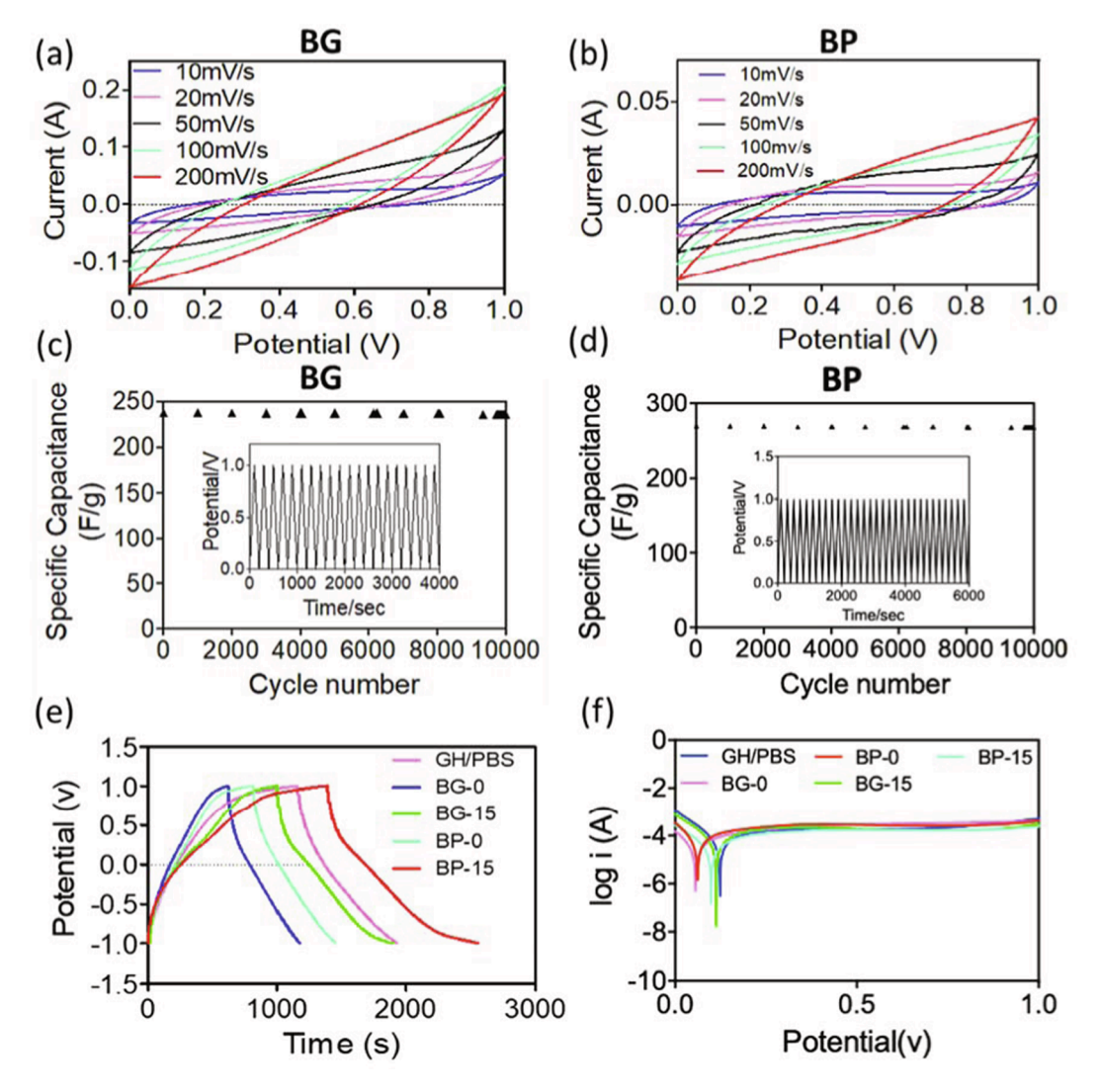


Fig. 3. Electrochemical performance of electrolytes. CV profile of (a) BG-15 and (b) BP-15 at different scan rates, voltage window 1 V, GH-L (Working electrode), Ag/AgCl (Reference electrode). Capacitance retention of (c) BG-15 and (d) BP-15 for up to 10,000 cycles. (e) Galvanostatic charge/discharge curve of GH-L (working electrode) and PBS, BG and BP (with 0% and 15% BIL loadings), as electrolyte at 0.1 A cm⁻³ and -1V to 1 V (f) Tafel plot of BG and BP hydrogels at 0 V-1 V.

enhancements are due to increase in electrostatic interactions with BIL functionalization which tethers the structure together, prevents uncoiling and chain slippage, slipping of chains leading to enhanced moduli. The increase in compressive strength can be attributed to bulky choline group's attachment to the structure and an increase in the overall molecular weight.

The extent of BIL functionalization and hydrogel crosslinking density are expected to bring about changes to fundamental physical properties of the gel electrolyte. This swelling and diffusive properties affect the shape and size of ion migration channels [39], which in turn are expected to influence electrochemical properties. Also, the electroactivity of the polymer-based hydrogels is associated with electrode–electrolyte interfacial transport, entailing ionic and electronic transport. Therefore, high porosity and interfacial areas are expected to be beneficial to electrochemical processing efficiency.

Evaluation of capacitance, power stability and CV of ink. Cyclic Voltammetry were performed at scan rates ranging from 10 to 200 mVs⁻¹ for both BG-15 (Fig. 3 a) and BP-15 (Fig. 3 b). The CV profiles were measured at different scan rates, using a voltage window of 1 V and employing GH-L as the working electrode and Ag/AgCl as the reference electrode.

The capacitance retention of BG-15 and BP-15 was determined for up to 10⁴ cycles (Fig. 3 c, d) at a scan rate of 50mVs⁻¹. The Galvanostatic charge-discharge curve of GH-L as working electrode and PBS and BG-15, BP-15 as well as BG-0 and BP-0 were determined at 0.1 A cm⁻³ and this is depicted in (Fig. 3 e). An increase of BIL concentration exhibits a well-defined discharge voltage plateau of \sim 0.5–0.8 V with a conductivity of $8.5 \times 10^{-4} - 3.5 \times 10^{-3} \text{ S m}^{-1}$ in both the polymers (Fig S4a). Gel electrolyte was tested as an electrochemical capacitor, based on GH-L, synthesized as electroactive material. Fig. 3 a and b indicates that the gel electrolyte BG-15 and BP-15 exhibit a specific capacitance of 238F g^{-1} and 262.90 Fg $^{-1}$ at a current density of 1 Ag $^{-1}$ in a three-electrode system from the calculations. The discharge current had a linear relationship with the scan rate at least up to 200 mVs⁻¹. The Tafel plot of the control - GH/PBS and those of the polymers BG-0, BG-15, BP-0 and BP-15 is shown in (Fig. 3 f) and discussed to understand the effect of BIL functionalization on the Faraday leakage current. An ideal polarizable electrode exhibits large change in voltage for a small change in current. Supercapacitors store large amounts of energy owing to thin double layer charge between porous plates soaked in electrolyte[40]. The porosity translates into a higher plate surface area conferring greater charge storing ability which in turn increases the charge-discharge cycles, a property, essential in small electronics. The surface area (158.836 m²/g) and the pore size distribution of the graphene hydrogel synthesized as shown in Fig. S3 upkeeps the charge storage ability. The primary disadvantage of supercapacitors is high leakage current causing self-discharge and energy dissipation over charge-discharge cycles. Redox reactions at the electrode - electrolyte interface cause electronic discharge through the double layer, known as the leakage current. This can be reduced by using an insulating thin film on the electrode surface, but it decreases the capacitance. The leakage current, understood based on the galvanostatic charge discharge cycles depends on the average redox potential of all possible faradaic reactions and the applied voltage, the difference of which is the overpotential and relates to the Tafel plot [41,42]. In (Fig. 3 f), the overpotential in significantly increased by BIL functionalization, almost to the level of a liquid, ionized electrolyte, emphasizing reduced leakage and enhanced storage efficiency with BIL functionalization.

Remarkably, the cycling performance of the electrolyte were obtained for 10,000 cycles. The electrolyte charged and discharged rapidly at a scan rate of 50 mVs $^{-1}$ with the maintenance of uniform capacitance indicating high instantaneous power. The ionic conductivity increases from $8\times 10^{-4}\pm 7\times 10^{-5}\,\mathrm{S}\,\mathrm{m}^{-1}$ to $15.3\times 10^{-3}\pm 3.3\times 10^{-4}\,\mathrm{S}\,\mathrm{m}^{-1}$ (Fig. S4 a) with increase of BIL concentration from 0 to 20 (w v $^{-1}$)%. The graphene hydrogel, studied versus glassy carbon electrode as working electrode, showed improved electrochemical performance with a nearly

rectangular shaped CV, indicating a typical double-layer capacitive behavior. The shape of CV curves in the scan rate range of 10-200 mV s⁻¹ indicate rapid transport or high electrolyte ion polarization and efficient charge transport on the electrode's surface[43], and the shape is retained indicating its excellent capacitance characteristics and reversibility in the experimental potential range. The absence of a sharp oxidation - reduction peak indicates that the electrolyte does not undergo oxidation or reduction process within the applied potential range [44-46]. This could be in part due to its complex and entangled polymeric structure, with the electrostatic polarization being different in different regions throughout the sample, where a differential continuum of hydration reigns over the structure. The reversibility of the specific capacitance is also indicated in (Fig. 3 c, d) which shows the specific capacitances over 10,000 cycles. In (Fig. S4 b) the variation in the current density with voltage for BG structures vis-a-vis BP structures pertains to the greater hydration and polarizability owing to the higher hydrophilic and polar nature of GelMA compared to the PEGDA main chain. At lower voltages, polarization causing the formation of the double layer prevents the current density from building up, but at higher voltages with the greater extent of intrinsic polar groups in the GelMA structure leads to higher current density in BG-15 than with BP-15 polymer at the same applied potential despite having the same concentration of BIL. The volumetric capacitance of BG-15 increases faster than BP-15 with scan rate as shown in (Fig. S4 c).

The CV curves at different scan rates (Fig. S5 a, b) and specific capacitance versus scan rate (Fig. S6-a, b) using GelMA and PEGDA with 0 to 20% BIL were determined. Lower scan rates aid electrolyte ion diffusion providing them with enough time for interaction with the electrode. Higher scan rates encourage surface accumulation. This is reflected for polymers with 0-10% BIL concentration. The diffusing species are water and hydrated BIL counter ions. The BIL pendant groups are thought to orient, towards the electrodes and provide for tunneling or interfering in hydrated BIL counter ion passage and transport. An anomaly is seen with an increase in the BIL from 15% to 20%, wherein the specific capacitance reduces with a further increase in BIL concentration to 20%. With a significantly high BIL concentration, a tight network due to electrostatic crosslinking is corroborated by swelling experiments. This tight network reduces diffusivity of the free BIL counter ions decreasing specific capacitance, volumetric capacitance at 200 mv s^{-1} is 294.17 \pm 2F cm^{-3} and 113.45 \pm 1F cm^{-3} for BG-15 and BP-15 respectively. The typical rectangular voltammogram of a capacitor is obtained from relation of current being proportional to the rate of change in voltage. However, hysteresis or memory in any process would result in an area enclosed within the forward and backward sweep curves as an indication of electrochemical activity. Capacitance can be explained through a Stern layer as the first, strongly adsorbed to the electrode immobile layer of BIL counter ions. The diffuse layer, beyond this first compact layer consists of ions under the influence of electrostatic forces and entropic diffusion and its potential slowly decreases with distance from the Stern layer. For a BIL functionalized polymer, the potential drop must consider the hydrated BIL ammonium which are oriented due to the application of potential. The representative electric circuit consists of electrode resistance, the Stern layer and diffuse layer capacitances in series [47,48].

Fig. S6 c shows the cyclic voltammetry of Graphene hydrogel and GH-L at a scan rate of 100 mV s⁻¹. The inclusion of laponite is expected to cause a decrease in capacitance due to the absence of solvated free ions that can account for the formation of the oriented Stern and diffuse layers [48,49]. (Fig. S7 - a) shows the Galvanostatic charge/discharge curve of BG-15 and BP-15 before and after polymerization. The charge discharge profile of ideal capacitors is triangular. In our case, the distortion from the ideal triangular shape could be due the build-up of pseudo capacitance while charging or electrolytic degradation. The two super capacitor charge storage mechanisms are electrostatic storage as the electrode surface double layer and faradaic storage at the electrode surface as pseudo capacitance [50]. The thermodynamics of the faradaic

charge transfer dictates that, a potential dependent charge storage and release occurs where the rate of charge storage versus applied voltage gives a measure of capacitance [18]. This charge transfer relates to reversible surface electrode reactions. The PBS electrolyte has the slowest rate of build-up of potential. As BIL% increases the rate of charge build up slows. As pendant group polarization progresses it becomes difficult to further polarize rationalizing the curved tip of the charging cycle. There is a nominal difference in galvanostatic charge discharge cycles of uncross linked prepolymer liquid and the crosslinked gel due to reduction in monomer segment and polymer chain mobility experienced during the pendant group orientation and de-orientation. The charge discharge cycles proffer an idea of the leakage current which depends on the average redox potential of faradaic reactions. The difference of the summation of these potentials from the applied voltage is the overpotential and this is indicated in the Tafel plots, as explained earlier, in (Fig. 3 f) [51-54]. The Tafel equation relates the faradaic reaction rate and leakage current with the applied voltage. The faraday reaction rate is controlled by kinetics and ion diffusion [55]. The overpotential at which this occurs comprises of the overpotentials for mass and charge transfers redox reactions and adsorption-desorption processes. It is used to find the exchange current as the intersection point between the cathodic and anodic slopes. It is advisable to avoid charging supercapacitors to voltages beyond the nominal redox overpotential to control the leakage [55,56]. However, energy density is proportional to charging voltage, a reduction in which decreases the stored energy of supercapacitors. The overpotential increases with BIL functionalization. This emphasized the enhancement in energy storage with BIL functionalization brought about by reduced leakage current. (Fig. S7 b) shows the Ragone plot comparing the BG-15 and BP-15 with different energy storage devices. The generic data ranges for other devices has reproduced from references [21]. In terms of power density, BG-15 and BP-15 are in the mid-range of the super capacitor spectrum with values ranging between 100 and 1200 W kg^{-1} for BG-15 400 to 1300 W kg^{-1} for BP-15. This implies that the materials can store large amounts of energy in a small mass, a property useful in miniature electronics applications. Both BG-15 MSC and BP-15 MSC exhibits exceptional energy and power density than existing biocompatible energy storage devices [57].

To further evaluate electrical performance, the frequency response of the supercapacitor with GH-L electrodes and BG-15, BP-15 electrolyte was analyzed by electrical impedance spectroscopy (EIS). Nyquist plots from EIS of the polymer electrolyte, with Glassy carbon electrode, at 0.1 V, are shown in (Fig. S8 a, b). The Nyquist of 20% (w v⁻¹) GelMA with varying concentration of BIL, with the inset shows the high-frequency regions is shown in (Fig. S8 a) while (Fig. S8 b) shows 20% (v v⁻¹) PEGDA with varying concentration of BIL. (Fig. S8 c) shows the Nyquist plot of BP-15 and BP-15-alginate material between 0.05 Hz and 1 MHz frequency. The curve's lower left portion corresponds to the higher frequency. For impedance spectroscopy on polymer electrolytes, the sample is considered as a parallel plate capacitor. An equivalent circuit entails a double layer capacitance electrolyte/electrode, in series with a film resistance and film capacitance in parallel with each other, which are in turn in series with a double layer capacitance [58,59]. However, neither of the components are pure elements given the depression of the semicircular region. The total impedance is related to oscillation frequencies for dipole and dielectric relaxation relating to local motion of the charged BIL pendant groups along the polymer chain. Permittivity and electric modulus, are related to the straight line on the Nyquist plots, represented by diffusion and electric relaxation from non-local flow of ions or solvent moieties [60]. The permittivity at very high frequencies, represents energy storage without hysteric dissipation. At low frequencies, permittivity represents dielectric loss which entails BIL group alignment, migration, polymer chain distortion, solvent convection and molecular vibration mediated energy dissipation. Supercapacitors are like resistance and capacitance at high and low frequencies respectively [58]. It is like a resistance-capacitance transmission line circuit in

interim frequencies, affected by electrode porosity, thickness and ion migration rates through the polymer hydrogel network. This shifts the low-frequency behavior towards resistive values. The plot is quite linear in this frequency range [61]. The depressed semicircle in the high-frequency region represented by interface charge transfer resistance and a double layer capacitance in parallel. The straight-line portion indicates Warburg impedance to local and global diffusion of free, ions through the polymeric network. A short Warburg region is due to increased ion diffusion [40,62].

Fabrication to construct flexible energy storage device and in-situ printing. Polymer /BIL composite as electrolyte and GH-L composite as electrode is been illustrated in (Fig. 4). In order to form a miniature implantable device, the electrolyte and electrode were 3D printed using ALLEVI 2, extrusion-based printing into different sized interdigitating structures. Laponite is a synthetic clay with 30 nm diameter and 1 nm thick disc-like particles [37]. The disks are negatively charged on the sides and on the edges, positive charged. It is well established that laponite dispersions are used in producing conductive, antistatic and barrier coatings [27,34]. Thus, the Laponite and graphene hydrogel mixture is been used as electrode in order to be able to print [63]. The storage and loss modulus of the mixture favors the printing. The interdigitating structure increases the interaction between the electrode and the electrolyte thus enhancing electrolytic process. (Fig. 4 a) shows the additive printing process for the energy storage device. The mass of the printed and air dried MSC is 26 mg (larger MSC) and 6 mg (smaller MSC). In both the structures, the electrolyte polymer makes up 74% by mass of the MSC structure, and the electrodes make up 26% of the MSC structure. (Fig. 4 b, c) show the prints, of various sizes, of BG-15 and BP-15 respectively. They illustrate the feature clarity that can be attained with the chosen composition and method of printing at different sizes. (Fig. 4 d) shows the variation of G' of BG-15 and BP-15 versus the oscillatory step time. With BG-15, the storage modulus (G') increases sharply with an increase in the rate of oscillatory stepping indicating the ability of the material to become stiffer with an increase in the rate of mechanical deformation. The rate of increase of G' for BG-0 is much slower. This indicates the formation of short length stress structures using hydrostatic and polar / electrostatic forces in the BG-0 structures, which due to orientation of the polymer chains prevents further slippage of chains and hence a rapid increase in the elastic modulus.

BP-15, on the other hand, owing to the chain structure of PEGDA contains a lower concentration of electrostatic forces tending to form the stress-oriented structure. Hence the elastic modulus builds up slowly with the oscillatory strain applied. In order to be able to print 3 wt% alginate was added to the BP-15 electrolyte, the CV curve shown in (Fig. S6 d, e) of BP-15 and BP-15-alginate reflects very similar values to that of the BG and BG-15. The cyclic voltammetry of the printed BG MSC (Fig. 4 e, f), using 1 V voltage window was performed to reveal the specific capacitance of printed device with varying interdigitation and the specific capacitance of the printed BP MSC (Fig. S6 e) with the current flow 3 orders of magnitude less than that of the electrode material is been indicated. The general characteristics of the material is reflected in the experimental values obtained with the printed design.

The printing parameters depend on the rheological properties of GH-L is illustrated in (Fig. S9a-d). Laponite, forms a thixotropic gel when dispersed in water. While the dynamic elastic modulus increases slightly with 3 and 6% Laponite (Fig. S9 a) with oscillatory step time, the G' as well as rate of increase with 9% Laponite is much higher. There is a minimum concentration that is needed to form a semi dilute overlapping region for the intercalated layers to interact and bond to each other. The 3% and 6% solutions are way below that concentration. The G' of 9% laponite with 1% Gelatin is much higher than that without gelatin (Fig. S9 b) which is due to the polar -polar interaction between the laponite and gelatin structures. (Fig. S9 c) shows the rheological properties of mixtures with varying percentage of graphene hydrogel with 9% Laponite. (Fig. S9-d) shows the rheology of the final compositions of laponite and graphene hydrogel composite-9% Laponite 7% Graphene

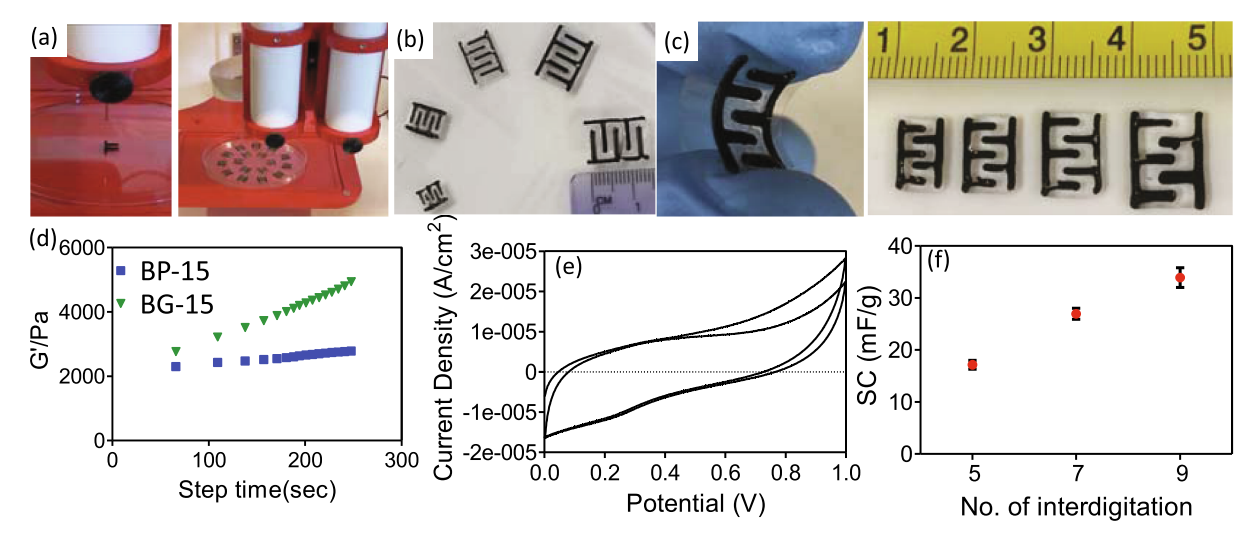


Fig. 4. 3D Printing of BG-15 electrolyte and GH-L electrode through a 0.51 mm nozzle using ALLEVI2 bioprinter (a) Image showing the printing process, additive printing of the energy storage device (b) Prints at various size of BG-15 (c) Prints at various size of BP-15, (d) Rheology of BG-15 and BP-15 (e) Cyclic Voltammetry curve with a voltage window of 0.1 V of the printed BG-15 supercapacitor with Ag/AgCl reference electrode (f) Specific capacitance of printed device with varying interdigitation and size.

hydrogel 1% Gelatin - chosen for printing. Also, 7% gelatin increases the G' of a 9% laponite dispersion, much more than 3% gelatin concentration. Again, the inter and intra component interactions are enhanced multifold in semi dilute regions while dilution beyond a certain level leads to a sudden decrease in the mutual polar and electrostatic interactions. The damping factor - tan delta, a ratio of G" / G' is<1 and decreases with the step time. The material is more "Solid" or "Gel" than "liquid" or "sol" and this tendency increases with increasing rates of deformation [63]. This is an important factor in choosing the right parameters for printing and ensuring structural integrity of the material in applications involving repetitive and oscillatory strains. In past few years graphene has been produced by chemically reducing graphene oxide (GO) or by graphene exfoliation or by chemical vapor deposition [64], and other common process for GO reduction was by employing hydrazine or its hydrate as reductant [65]. However, hydrazine's toxic and explosive characteristics precludes its use in biocompatible device fabrication. Graphene aerogel has been synthesized using the non-toxic ascorbic acid as reducing agent, L-Ascorbic acid (L-AA) [66]. The device can be fabricated into different shapes and sizes thus making it versatile according to the need, the number of interdigitations was varied to check the capacitance of the device. The specific capacitance of the printed device with 5 interdigitations being $17.16\pm0.83\mu F~g^{-1}$ increases to $33.9\pm1.9~\mu F~g^{-1}$ with the increase in the interdigitations as indicated in (Fig. 4 f). Thus, the performance of the printed energy storage device depends on the size of the device. In order to estimate the capacitance retention of the printed device in~vivo, the device was explanted after day 4 of implantation and capacitance was measured as $19.90\pm0.20\mu F~g^{-1}$ indicating an increase in the capacitance $17.16\pm0.83\mu F~g^{-1}$ before implanting (Fig. 6 k).

In order to estimate the ability to integrate the printed device to *in vivo* applications, the device was printed on porcine skin, both the electrode (9% Laponite 7% Graphene hydrogel 1% Gelatin) and electrolyte (BG- 15) were 3D printed in various shape on epidermal layer of the skin (Fig. 5). For the first time, proof-of-concept has been demonstrated utilizing a printable 3D biocompatible graphene-based energy storage device that has been 3D printed on tissue. Additionally, this 3D

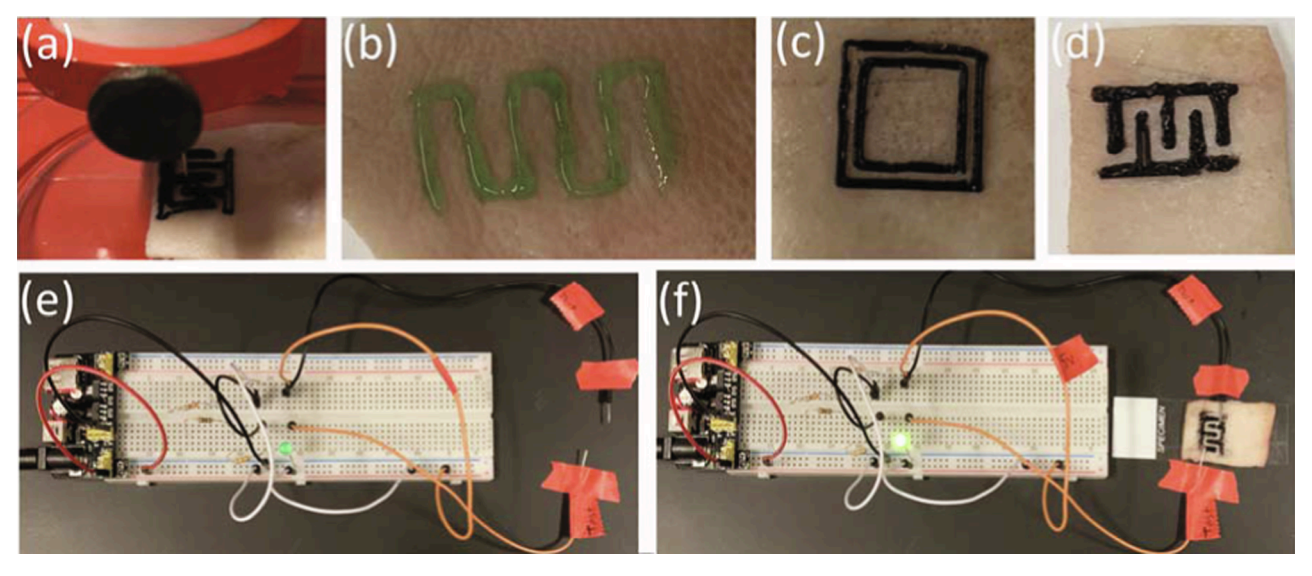


Fig. 5. Printing of Energy storage device through a 0.51 mm nozzle using ALLEVI2 bioprinter on Porcine skin (a) Image showing the printing process (b) BG-15 electrolyte (c) GH-L electrode (d) Energy storage device (e) Breadboard setup to validate the conductivity of the printed device (f) 3D-printed energy storage device connected to the 1 V power source to illuminate the LED.

printed device platform has been analyzed towards its ability to illuminate an LED at 1 V of input current and exhibit a steady output (Fig. 5 e,f). Practical applications in *in vivo* environments of a device entails being subject to mechanical stress evaluation of fabricated energy storage device under mechanical deformation as an important parameter. The results are shown in Figure S10. (Fig. S10 a-b) shows the digital image of the fabricated device connected to a bread board set up to indicate successful illumination of LED before and after deformation. (Fig. S10 c) compares the cyclic voltammetry of the device before and after bending at a voltage window of 0–1 V. (Fig S10 d-e) show the digital image of elastic modulus study on the device, while (Fig S10 f) shows the mechanical stability of the fabricated energy storage device, underscoring its structural stability under mechanical stress.

Previously, Zhao et al has shown the 3D printing periodic graphene-based composite hybrid aerogel microlattices. similarly we count on this platform as the basis of futuristic 3D printed energy storage device that can be used in many biomedical and tissue engineering applications as a free-standing energy storage platform[67-69]. This process of 3D printing of our device made up of BIL, directly on the epidermal layer overcomes the limitation of current polymers electrolyte not being able to have enhanced adhesion. For further establishment of in situ 3D printing, the organ and body motion along with the print head movement needs to be taken into consideration for optimal results, previously researchers have demonstrated 3D printing of keratinocytes and fibroblasts in stratified zones throughout the wound bed to fill a skin lesion. Also, advancements in robotic bioprinters and robot-assisted surgery may also be integral to the evolution of this technology in the future [70,71].

In vitro and In vivo viability of the flexible electrolyte. To investigate the potential of BG-15 and BG-MSC to support the growth and spreading in 2D cultures *in vitro*, the viability and metabolic activity of C2C12 cells growing on the surface of the electrolyte and fabricated energy storage device was determined over a culture period of 7 days (Fig. S11 a-g).

Viability of seeded cells on electrolyte and MSC was not affected due to the presence of the BIL. Cells seeded on the surface of BG-15 and BG-MSC appeared to exhibit 91.6% $\pm1.44\%$ and 91.8% $\pm0.6\%$ survival rates, respectively, one day post-seeding. Furthermore, primary cultures increased their metabolic activity consistently through the duration of the culture, during the day one post seeding were 4467.3 \pm 18 RFU and 4624.02 \pm 44 RFU for BG-15 and BG-MSC respectively which increased to 10450.25 \pm 414 RFU and 11545.14 \pm 596 RFU as shown indicating the unaffected metabolic activity. In addition, electrolyte contained higher cell numbers than the fabricated device at day 7 post-seeding, as seen by DAPI-stained cell nuclei quantification

In vivo biocompatibility of conventional electrolytes and energy storage devices are often a key limitation that hinders safe implantation as these implants often trigger a persistent inflammatory response owing to prolonged half-lives in the organism [72]. In this study we investigated the in vivo degradation and interactions of 3D printed energy storage device BG-MSC and BP-MSC with local tissues. We also looked at the immunogenicity profile as subcutaneously implants in an animal. Explanted samples, at days 4, 14, and 28 post-implantations, showed that electrolyte and energy storage device showed sustained biodegradation through the 28 days of implantation (Fig. 6 a-d). Also, in the CD68 staining when compared to control and day 4 staining, day 28 showed to have a low number of monocytes (Fig. 6 e-h). This observation suggests that the printed device was efficiently degraded in vivo, potentially by enzymatically hydrolyzing the hydrogel matrix. Furthermore, polymer/BIL conjugation at different ratios could be employed for engineering electroconductive hydrogels with varying degrees of biodegradability. In vivo biocompatibility and degradation of BP-MSC is shown in (Fig. S12). Hematoxylin and eosin (H&E) staining of printed device and surrounding tissue is shown in (Fig. S11 a-d) for control and after 4, 14 and 28 days of implantation. (Fig. S12 e-h) shows the fluorescent immunohistochemical analysis, macrophage (CD68) presence counterstained with nuclei (DAPI) for control and after 4, 14,

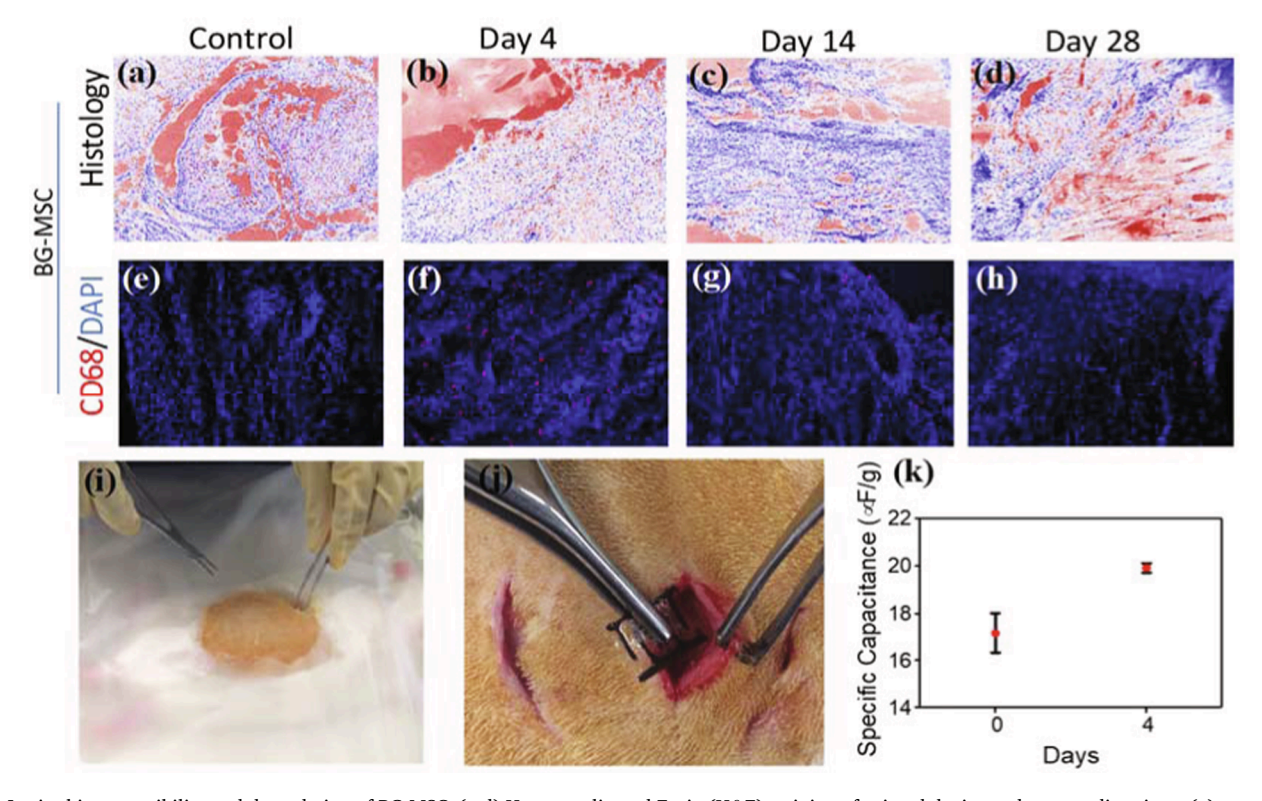


Fig. 6. In vivo biocompatibility and degradation of BG-MSC. (a-d) Hematoxylin and Eosin (H&E) staining of printed device and surrounding tissue (a) control (b) 4 days, (c) 14 days, and (d) 28 days of implantation (e-h) Fluorescent immunohistochemical analysis, macrophage (CD68) presence (e) control (f) 4 days, (g) 14 days, and (h) 28 days counterstained with nuclei (DAPI) (i,j) Image of subcutaneous supercapacitor implantation. (k) Specific capacitance of the printed device before and at day 4 after implantation.

and 28 days of implantation.

4. Conclusion

In summary, we developed a novel material platform of bio compatible polymer electrolytes for MSCs. Conjugation of BIL-choline functionality on Gelatin biopolymer and synthetic PEGDA polymer was seen to significantly enhance capacitive and mechanical properties, achieving high cycle stability and material energy densities nearly as high as batteries without any compromising power densities. Additionally, the bio compatibility accentuates its application potential in bio implantable devices. We optimized the rheological and electromechanical properties of GH-L blend for use as highly conductive electrode, thus combining the novel polymer electrolyte materials with the GH-L electrodes for scalable 3D printing of interdigitated miniaturized supercapacitor structures and showed the feasibility of high-charge storage capacity. The ability of the electrolyte to penetrate the porous high surface are electrode gives these MSC devices high capacitance retention and high power and energy density. Additionally, enhanced mechanical stability of the electrolyte due to BIL functionalization made it stronger and easier to fabricate. The fabricated, biocompatible and biodegradable supercapacitor can be used in implantable device applications which require high cycle stability and high-power density. In summation, we designed a novel material platform technology for inducing tailorable specific capacitance and other electromechanical properties onto bio polymer and biocompatible synthetic polymers, intended for use as solid state electrolytes. The interdigitated 3D printed MSC structures using these materials showed great promise with respect to their biocompatibility and electrochemical properties bespeak their robustness and capability of scalable applications in bio-implantable microelectronics and further as robust energy storage structures for sensors and actuators.

Declaration of Competing Interest

The authors declare that they have no known competing financial interests or personal relationships that could have appeared to influence the work reported in this paper.

Acknowledgements

This work was supported by NSF grant numbers: 1919092 and 2005317, New Jersey Health Foundation and Camden Health Initiative Funding.

Appendix A. Supplementary data

Supplementary data to this article can be found online at https://doi. org/10.1016/j.cej.2020.128213.

References

- [1] Y.R. Jeong, G. Lee, H. Park, J.S. Ha, Stretchable, Skin-Attachable Electronics with Integrated Energy Storage Devices for Biosignal Monitoring, Acc. Chem. Res. 52 (1) (2019) 91–99, https://doi.org/10.1021/acs.accounts.8b00508.
- [2] Y. Chen, Y. Zhang, Z. Liang, Y.u. Cao, Z. Han, X. Feng, Flexible inorganic bioelectronics, npj Flex Electron. 4 (1) (2020), https://doi.org/10.1038/s41528-020-0065-1.
- [3] Y. Song, J. Min, W. Gao, Wearable and Implantable Electronics: Moving toward Precision Therapy, ACS Nano 13 (2019) 12280–12286.
- [4] Y. Liu, M. Pharr, G.A. Salvatore, Lab-on-Skin: A Review of Flexible and Stretchable Electronics for Wearable Health Monitoring, ACS Nano 11 (2017) 9614–9635.
- [5] C.L. Ventola, Medical Applications for 3D Printing: Current and Projected Uses, P T 39 (2014) 704–711.
- [6] J.K. Placone, A.J. Engler, Recent Advances in Extrusion-Based 3D Printing for Biomedical Applications, Adv. Healthcare Mater. 7 (8) (2018) 1701161, https://doi.org/10.1002/adhm.201701161.
- [7] S. Waheed, J.M. Cabot, N.P. Macdonald, T. Lewis, R.M. Guijt, B. Paull, M. C. Breadmore, 3D printed microfluidic devices: enablers and barriers, Lab Chip 16 (11) (2016) 1993–2013, https://doi.org/10.1039/C6LC00284F.

- [8] P.S. Gungor-Ozkerim, I. Inci, Y.S. Zhang, A. Khademhosseini, M.R. Dokmeci, Bioinks for 3D bioprinting: an overview, Biomater. Sci. 6 (5) (2018) 915–946, https://doi.org/10.1039/C7BM00765E.
- [9] J. Gopinathan, I. Noh, Recent trends in bioinks for 3D printing, Biomater Res 22 (1) (2018), https://doi.org/10.1186/s40824-018-0122-1.
- [10] M.S. Brown, B. Ashley, A. Koh, Wearable Technology for Chronic Wound Monitoring: Current Dressings Advancements, and Future Prospects, Front Bioeng. Biotechnol. 6 (2018) 47.
- [11] H. Yuk, B. Lu, X. Zhao, Hydrogel bioelectronics, Chem. Soc. Rev. 48 (6) (2019) 1642–1667, https://doi.org/10.1039/C8CS00595H.
- [12] C. Lethien, J. Le Bideau, T. Brousse, Challenges and prospects of 3D microsupercapacitors for powering the internet of things, Energy Environ. Sci. 12 (1) (2019) 96–115, https://doi.org/10.1039/C8EE02029A.
- [13] J.-C. Li, J. Gong, Z. Yang, Y. Tian, X. Zhang, Q. Wang, X. Hong, Design of 2D Self-Supported Hybrid CuSe@PANI Core/Shell Nanosheet Arrays for High-Performance Flexible Microsupercapacitors, J. Phys. Chem. C 123 (48) (2019) 29133–29143, https://doi.org/10.1021/acs.jpcc.9b08889.s003.
- [14] J. Wang, V.K. Bandari, D. Karnaushenko, Y. Li, F. Li, P. Zhang, S. Baunack, D. D. Karnaushenko, C. Becker, M. Faghih, T. Kang, S. Duan, M. Zhu, X. Zhuang, F. Zhu, X. Feng, O.G. Schmidt, Self-Assembly of Integrated Tubular Microsupercapacitors with Improved Electrochemical Performance and Self-Protective Function, ACS Nano 13 (7) (2019) 8067–8075, https://doi.org/10.1021/acsnano.9b02917.s003.
- [15] W.A. Haider, L. He, H.A. Mirza, M. Tahir, A.M. Khan, K.A. Owusu, W. Yang, Z. Wang, L. Mai, Bilayered microelectrodes based on electrochemically deposited MnO2/polypyrrole towards fast charge transport kinetics for microsupercapacitors, RSC Advances 10 (2020) 18245-18251.
- [16] V.S. Mallela, V. Ilankumaran, N.S. Rao, Trends in cardiac pacemaker batteries, Indian Pacing Electrophysiol. J. 4 (2004) 201–212.
- [17] L.A. Geddes, R. Roeder, Criteria for the Selection of Materials for Implanted Electrodes, Annal. Biomedical. Eng. 31 (7) (2003) 879–890, https://doi.org/ 10.1114/1.1581292.
- [18] J. Liu, J. Wang, C. Xu, H. Jiang, C. Li, L. Zhang, J. Lin, Z.X. Shen, Advanced Energy Storage Devices: Basic Principles, Analytical Methods, and Rational Materials Design, Adv. Sci. (Weinh) 5 (2017) 1700322.
- [19] M. Beidaghi, Y. Gogotsi, Capacitive energy storage in micro-scale devices: recent advances in design and fabrication of micro-supercapacitors, Energy Environ. Sci. 7 (2014) 867–884.
- [20] H.D. Yoo, E. Markevich, G. Salitra, D. Sharon, D. Aurbach, On the challenge of developing advanced technologies for electrochemical energy storage and conversion, Mater. Today 17 (3) (2014) 110–121, https://doi.org/10.1016/j. mattod.2014.02.014.
- [21] M. Winter, R.J. Brodd, What Are Batteries, Fuel Cells, and Supercapacitors? Chem. Rev. 104 (10) (2004) 4245–4270, https://doi.org/10.1021/cr020730k.
- [22] Z. Wang, S.J. Lee, H.-J. Cheng, J.J. Yoo, A. Atala, 3D bioprinted functional and contractile cardiac tissue constructs, Acta Biomater. 70 (2018) 48–56, https://doi. org/10.1016/j.actbio.2018.02.007.
- [23] M. Qasim, F. Haq, M.-H. Kang, J.-H. Kim, 3D printing approaches for cardiac tissue engineering and role of immune modulation in tissue regeneration, Int. J. Nanomed. 14 (2019) 1311–1333.
- [24] S.R. Shin, S.M. Jung, M. Zalabany, K. Kim, P. Zorlutuna, S.B. Kim, M. Nikkhah, M. Khabiry, M. Azize, J. Kong, K.-T. Wan, T. Palacios, M.R. Dokmeci, H. Bae, X. (. Tang, A. Khademhosseini, Carbon-Nanotube-Embedded Hydrogel Sheets for Engineering Cardiac Constructs and Bioactuators, ACS Nano 7 (3) (2013) 2369–2380, https://doi.org/10.1021/nn305559j.
- [25] Y. Xu, Z. Lin, X. Huang, Y. Liu, Y.u. Huang, X. Duan, Flexible Solid-State Supercapacitors Based on Three-Dimensional Graphene Hydrogel Films, ACS Nano 7 (5) (2013) 4042–4049, https://doi.org/10.1021/nn4000836.
- [26] S. Stankovich, D.A. Dikin, G.H.B. Dommett, K.M. Kohlhaas, E.J. Zimney, E. A. Stach, R.D. Piner, S.T. Nguyen, R.S. Ruoff, Graphene-based composite materials, Nature 442 (7100) (2006) 282–286, https://doi.org/10.1038/nature04969.
- [27] D.W. Thompson, J.T. Butterworth, The nature of laponite and its aqueous dispersions, J. Colloid Interface Sci. 151 (1) (1992) 236–243, https://doi.org/ 10.1016/0021-9797(92)90254-J.
- [28] D.C. Marcano, D.V. Kosynkin, J.M. Berlin, A. Sinitskii, Z. Sun, A. Slesarev, L. B. Alemany, W. Lu, J.M. Tour, Improved Synthesis of Graphene Oxide, ACS Nano 4 (8) (2010) 4806–4814, https://doi.org/10.1021/nn1006368.
- [29] J.W. Nichol, S.T. Koshy, H. Bae, C.M. Hwang, S. Yamanlar, A. Khademhosseini, Cell-laden microengineered gelatin methacrylate hydrogels, Biomaterials 31 (21) (2010) 5536–5544, https://doi.org/10.1016/j.biomaterials.2010.03.064.
- [30] S.H. Zeisel, K.-A. da Costa, Choline: an essential nutrient for public health, Nutr. Rev. 67 (2009) 615–623.
- [31] B.L. Gadilohar, G.S. Shankarling, Choline based ionic liquids and their applications in organic transformation, J. Mol. Liquids 227 (2017) 234–261, https://doi.org/ 10.1016/j.molliq.2016.11.136.
- [32] I. Noshadi, B.W. Walker, R. Portillo-Lara, E. Shirzaei Sani, N. Gomes, M. R. Aziziyan, N. Annabi, Engineering Biodegradable and Biocompatible Bio-ionic Liquid Conjugated Hydrogels with Tunable Conductivity and Mechanical Properties, Sci Rep 7 (2017) 4345.
- [33] S. Gallagher, L. Florea, K. Fraser, D. Diamond, Swelling and Shrinking Properties of Thermo-Responsive Polymeric Ionic Liquid Hydrogels with Embedded Linear pNIPAAM, Int. J. Mol. Sci. 15 (2014) 5337.
- [34] A.V. Dobrynin, Theory and simulations of charged polymers: From solution properties to polymeric nanomaterials, Current Opinion in Colloid & Interface Science 13 (2008) 376-388.

- [35] M. Kamli, M. Guettari, T. Tajouri, Structure of polyvinylpyrrolidone aqueous solution in semi-dilute regime: Roles of polymer-surfactant complexation, J. Mol. Struct. 1196 (2019) 176–185.
- [36] T. Canal, N.A. Peppas, Correlation between mesh size and equilibrium degree of swelling of polymeric networks, J. Biomed. Mater. Res. 23 (10) (1989) 1183–1193, https://doi.org/10.1002/jbm.820231007.
- [37] Q. Chai, Y. Jiao, X. Yu, Hydrogels for Biomedical Applications: Their Characteristics and the Mechanisms behind Them, Gels 3 (2017) 6.
- [38] S.-V.-F. Fariba Ganji, E. Vasheghani-Farahani, Theoretical Description of Hydrogel Swelling: A Review, Iranian Polym. J. (2010).
- [39] S.T. Koshy, T.C. Ferrante, S.A. Lewin, D.J. Mooney, Injectable, porous, and cell-responsive gelatin cryogels, Biomaterials 35 (8) (2014) 2477–2487, https://doi.org/10.1016/j.biomaterials.2013.11.044.
- [40] J.E.B. Randles, Kinetics of rapid electrode reactions, Discuss. Faraday Soc. 1 (1947) 11, https://doi.org/10.1039/df9470100011.
- [41] I.S. Ike, I. Sigalas, S. Iyuke, Understanding performance limitation and suppression of leakage current or self-discharge in electrochemical capacitors: a review, Phys. Chem. Chem. Phys. 18 (2) (2016) 661–680, https://doi.org/10.1039/ C5CP054594
- [42] J.H. Min, M. Patel, W.-G. Koh, Incorporation of Conductive Materials into Hydrogels for Tissue Engineering Applications, Polymers (Basel) 10 (2018) 1078.
- [43] H. Peng, G. Ma, K. Sun, Z. Zhang, Q. Yang, F. Ran, Z. Lei, A facile and rapid preparation of highly crumpled nitrogen-doped graphene-like nanosheets for highperformance supercapacitors, J. Mater. Chem. A 3 (25) (2015) 13210–13214, https://doi.org/10.1039/C5TA03034J.
- [44] P. Tamilarasan, S. Ramaprabhu, Graphene based all-solid-state supercapacitors with ionic liquid incorporated polyacrylonitrile electrolyte, Energy 51 (2013) 374–381, https://doi.org/10.1016/j.energy.2012.11.037.
- [45] K.J.R. Noemie Elgrishi, Brian D. McCarthy, Eric S. Rountree, Thomas T. Eisenhart, and Jillian L. Dempsey*, A Practical Beginner's Guide to Cyclic Voltammetry, J. Chem. Educ (2018).
- [46] Tae Young Kim, Hyun Wook Lee, Meryl Stoller, Daniel R. Dreyer, Christopher W. Bielawski, Rodney S. Ruoff, Kwang S. Suh, High-Performance Supercapacitors Based on Poly(ionic liquid)-Modified Graphene Electrodes, ACS Nano 5 (1) (2011) 436–442, https://doi.org/10.1021/nn101968p.
- [47] Y.J.-W. Tian Ying, X.U.E. Rong, Y.I. Bao-Lian, Influence of Electrolyte Concentration and Temperature on the Capacitance of Activated Carbon, Acta Phys. Chim. Sinica 27 (2011) 479–485.
- [48] Matthew A. Brown, Alok Goel, Zareen Abbas, Effect of Electrolyte Concentration on the Stern Layer Thickness at a Charged Interface, Angew. Chem. Int. Ed. 55 (11) (2016) 3790–3794. https://doi.org/10.1002/anie.201512025.
- [49] Hainan Wang, Laurent Pilon, Accurate Simulations of Electric Double Layer Capacitance of Ultramicroelectrodes, J. Phys. Chem. C 115 (33) (2011) 16711–16719, https://doi.org/10.1021/jp204498e.
- [50] P. Iamprasertkun, C. Tanggarnjanavalukul, A. Krittayavathananon, J. Khuntilo, N. Chanlek, P. Kidkhunthod, M. Sawangphruk, Insight into charge storage mechanisms of layered MnO2 nanosheets for supercapacitor electrodes: In situ electrochemical X-ray absorption spectroscopy, Electrochim. Acta 249 (2017) 26–32.
- [51] X. Jiang, J. Polastre, D. Culler, Perpetual environmentally powered sensor networks, IPSN 2005. Fourth International Symposium on Information Processing in Sensor Networks, 2005., 2005, pp. 463-468.
- [52] Andrew Burke, Ultracapacitors: why, how, and where is the technology, J. Power Sour. 91 (1) (2000) 37–50, https://doi.org/10.1016/S0378-7753(00)00485-7.
- [53] Patrice Simon, Yury Gogotsi, Materials for electrochemical capacitors, Nature Mater 7 (11) (2008) 845–854, https://doi.org/10.1038/nmat2297.

- [54] V.V.N. Obreja, On the performance of supercapacitors with electrodes based on carbon nanotubes and carbon activated material—A review, Phys. E: Low-Dimensional Syst. Nanostruct. 40 (2008) 2596-2605.
- [55] A. Slesinski, C. Matei-Ghimbeu, K. Fic, F. Béguin, E. Frackowiak, Self-buffered pH at carbon surfaces in aqueous supercapacitors, Carbon 129 (2018) 758-765.
- [56] Z. Dai, C. Peng, J.H. Chae, K.C. Ng, G.Z. Chen, Cell voltage versus electrode potential range in aqueous supercapacitors, Sci. Rep. 5 (2015) 9854-9854.
- [57] B.E. Layton, A Comparison of Energy Densities of Prevalent Energy Sources in Units of Joules Per Cubic Meter, Int. J. Green Energy 5 (6) (2008) 438–455, https://doi.org/10.1080/15435070802498036.
- [58] P.L. Taberna, P. Simon, J.F. Fauvarque Electrochemical Characteristics and Impedance Spectroscopy Studies of Carbon-Carbon Supercapacitors, Journal of The Electrochemical Society 150 (2003) A292-A300.
- [59] S.B. Aziz, T.J. Woo, M.F.Z. Kadir, H.M. Ahmed, A conceptual review on polymer electrolytes and ion transport models, J. Sci. Adv. Mater. Dev. 3 (1) (2018) 1–17, https://doi.org/10.1016/j.jsamd.2018.01.002.
- [60] M. Coşkun, Ö. Polat, F.M. Coşkun, Z. Durmuş, M. Çağlar, A. Türüt, The electrical modulus and other dielectric properties by the impedance spectroscopy of LaCrO3 and LaCrO.90Ir0.10O3 perovskites, RSC Advances 8 (2018) 4634-4648.
- [61] D. Qu, H. Shi, Studies of activated carbons used in double-layer capacitors, J. Power Sources 74 (1) (1998) 99–107, https://doi.org/10.1016/S0378-7753(98) 00038-X.
- [62] M.D. Stoller, S. Park, Y. Zhu, J. An, R.S. Ruoff, Graphene-Based Ultracapacitors, Nano Lett. 8 (10) (2008) 3498–3502, https://doi.org/10.1021/nl802558y.
- [63] W. Huang, Y. Wu, L. Qiu, C. Dong, J. Ding, D. Li, Tuning Rheological Performance of Silica Concentrated Shear Thickening Fluid by Using Graphene Oxide, Adv. Conden. Matter Phys. 2015 (2015) 5.
- [64] M.S.A Bhuyan, M.N. Uddin, M.M. Islam, F.A. Bipasha, S.S. Hossain, Synthesis of graphene, Int Nano Lett 6 (2) (2016) 65–83, https://doi.org/10.1007/s40089-015-0176-1.
- [65] S. Park, J. An, J.R. Potts, A. Velamakanni, S. Murali, R.S. Ruoff, Hydrazinereduction of graphite- and graphene oxide, Carbon 49 (9) (2011) 3019–3023, https://doi.org/10.1016/j.carbon.2011.02.071.
- [66] H.Y. Jiali Zhang, Guangxia Shen, Ping Cheng, Jingyan Zhang and Shouwu Guo, Reduction of graphene oxide via L-ascorbic acid, Chem. Commun., (2010).
- [67] J. Zhao, Y. Zhang, X. Zhao, R. Wang, J. Xie, C. Yang, J. Wang, Q. Zhang, L. Li, C. Lu, Y. Yao, Direct Ink Writing of Adjustable Electrochemical Energy Storage Device with High Gravimetric Energy Densities, Adv. Funct. Mater. 29 (2019) 1900809
- [68] J. Zhao, Y. Zhang, Y. Huang, X. Zhao, Y. Shi, J. Qu, C. Yang, J. Xie, J. Wang, L. Li, Q. Yan, S. Hou, C. Lu, X. Xu, Y. Yao, Duplex printing of all-in-one integrated electronic devices for temperature monitoring, J. Mater. Chem. A 7 (3) (2019) 972–978, https://doi.org/10.1039/C8TA09783F.
- [69] J. Zhao, Y. Zhang, Y. Huang, J. Xie, X. Zhao, C. Li, J. Qu, Q. Zhang, J. Sun, B. He, Q. Li, C. Lu, X. Xu, W. Lu, L. Li, Y. Yao, 3D Printing Fiber Electrodes for an All-Fiber Integrated Electronic Device via Hybridization of an Asymmetric Supercapacitor and a Temperature Sensor, Adv. Sci. 5 (2018) 1801114.
- [70] I.T. Ozbolat, Y. Yu, Bioprinting toward organ fabrication: challenges and future trends, IEEE Trans Biomed Eng 60 (2013) 691-699.
- [71] X. Cui, T. Boland, D.D. D'Lima, M.K. Lotz, Thermal inkjet printing in tissue engineering and regenerative medicine, Recent Pat. Drug Deliv. Formul. 6 (2012) 149–155.
- $\ \ \,$ [72] K. Bazaka, M.V. Jacob, Implantable Devices: Issues and Challenges, Electronics 2 (2013) 1–34.